IX. BOUNDARY PHYSICS

D. N. HILL (LLNL), B. BRAAMS (NYU), J. HAINES (McDonnell-Douglas), J. MILOVICH (LLNL), T. ROGNLIEN (LLNL), D. P. STOTLER (PPPL), and M. ULRICKSON (PPPL)

IX.A. INTRODUCTION

In this chapter, we focus on the physics basis for the expected operating conditions at the BPX divertor and inner wall limiter. The essential features of the BPX device have been fully described in previous chapters. The main reasons for choosing the divertor configuration are the desire to obtain H-mode operation with high confinement and to obtain "high-recycling" operation in which a high-density, low-temperature plasma is formed in front of the target plates so as to minimize sputtering and impurity transport back to the core plasma. It is planned for BPX to operate primarily in the double–null (DN) configuration to maximize the contact area for heat removal. However, upper and lower single–null (SN) operation is also possible to minimize the H-mode power threshold. Inner-wall limiter configurations can also be obtained to provide a further option for increasing the power handling capabilities of the device.

In terms of the plasma conditions in the scrape–off layer (SOL), BPX represents a significant extrapolation from present machines because of its high power and relatively compact size. It also operates at more than twice the toroidal field of any other operating divertor tokamak. Table 9.1 gives a comparison between BPX and other tokamaks in terms of expected heat flux across the separatrix and at the divertor targets. (In the table, A_p is the plasma surface area, V_p the volume, and A_{div} the actual contact area at the divertor targets.) With 17 MW of ion cyclotron resonance frequency (ICRF) + ohmic heating (OH) power, BPX could produce 420 MW of fusion power at $Q = 25$. Then $P_{loss} = 0.2 \times Q + P_{ICH} = 100$ MW should be deposited in the plasma and must be lost by radiation to the walls and conduction to the divertor plates. The peak divertor heat flux at the end of the $Q = 25$ burn phase ($\sim$20 MW/m^2 exclusive of toroidal peaking factors) is expected to be higher than values in most present tokamaks[1–3]: $\simeq$30 MW/m^2 in JET, $\simeq$5 MW/m^2 in JT–60 and DIII–D. At $Q = 5$ with $P_{fus} = 100$ MW and $P_{loss} = 40$ MW, the peak divertor heat flux will be down to about 12 MW/m^2. Active sweeping of the X–points will be used to reduce the temperature rise to manageable levels for inertially cooled divertor targets.

The predicted operating conditions at the divertor are derived primarily from numerical simulations using the B2 code,[4] similar to the approach of the NET, INTOR, and ITER design groups. Simulation is required because of the scarcity of systematic experimental studies[5,6] showing the scaling of key SOL plasma parameters with core parameters such as I_p, P_{heat}, B_T, or $\bar{n}_e$, none of which have been able to be carried out at energy fluxes comparable to BPX. The codes employed solve the fully two-dimensional problem of SOL transport using a realistic magnetic geometry and input assumptions for plasma transport based on comparisons with experimental data on other tokamaks. Much of the effort in this field is also directly applicable to ITER, and so a number of people are working on studies for both devices. This is good because we are, in effect, pooling our resources on the common problems of divertor design.

The SOL plasma simulations predict a peak divertor heat flux for $Q = 25$ operation in the 17 to 30 MW/m^2 range, depending primarily on (a) the distribution of power among the four strike-points, (b) the value of the thermal diffusivity ($\chi_{i,e}$ for ions, electrons) in the SOL plasma, (c) the magnetic flux expansion at the divertor targets, and (d) radiative losses in the edge plasma. Peak electron temperatures at the targets ($T_{e,div}$) are predicted to lie in the 30- to 100-eV range. This result is important because the the sputtering rate and target plate erosion are strongly temperature dependent. Unfortunately, the uncertainty here is relatively large because $T_{e,div}$ is sensitive to even more parameters than is the heat flux: In addition to $D_\perp$ and χ_e, the recycling coefficient directly affects it. Lower uncertainties for $T_{e,div}$ await better experimental data from existing tokamaks.

IX.B. DIVERTOR GEOMETRY

Most BPX operation will use the double-null open divertor geometry of Fig. 9.1, that will allow for radial sweeping of X–point position. This geometry is very similar to that found in other open divertor tokamaks that have obtained H mode: DIII, DIII–D, JET, JFT–2M, JT–60, and PBX. In these devices, the divertor plasma itself provides the necessary gas shielding. The exact degree of "openness" (or the ability of recycled neutrals from the divertor to fuel the core plasma) allowed is still

Table 9.1. Expected BPX Parameters Compared to Other Tokamaks

Power Density	ASDEX	DIII-D	JET	BPX	ITER
$\frac{P_{in}}{V_p}\left(\frac{\text{MW}}{\text{m}^3}\right)$	0.8	0.9	0.12	1.5	0.2
$\frac{P_{SOL}}{A_p}\left(\frac{\text{MW}}{\text{m}^2}\right)$	0.12	0.24	0.06	0.61	0.14
$\frac{P_{div}}{A_{div}}\left(\frac{\text{MW}}{\text{m}^2}\right)$	2.5	1.2–5	23	20	11
$P_{d,meas}$ (MW/m^2)	2.5	4	30	N/A	N/A
Core Density					
$\bar{n}_e$ (10^{20} m^{-3})	0.3–0.7	0.6–1.4	0.6	3.0	0.7–1.5
Divertor Density					
$n_{e,d}$ (10^{20} m^{-3})	0.5	0.3–2.0	0.3	2–3	3–7
Loss Energy	Assuming $\tau_p = 2\ \tau_E$ H-mode				
$\frac{Q_{SOL}}{\Gamma_{sep}}\left(\frac{\text{keV}}{\text{ion}}\right)$	12.5	3.5	10	26	52

not well understood. However, JET, DIII-D, and JFT-2M all report good H-mode confinement even with the X-point on or slightly outside the first-wall surface[7,8] (i.e., a minimum of plasma shielding). Therefore, no divertor baffling is planned for BPX.

Determining the optimum distance from the X-point to the target plates ($L_{p,d}$ in the poloidal plane and $L_{\|,d}$ along the field lines) involves several trade-offs. First, the desire to keep the edge magnetic $q \geq 3.2$ (for stability and confinement) pushes us in the direction of small $L_{p,d}$. Second, the desire to lower the peak divertor heat flux $\hat{q}_d$ also drives us to reduce $L_{p,d}$ to take advantage of the flux expansion near the null, though X-point sweeping and more stringent requirements for tile alignment (the field lines are more nearly toroidal near the null) reduce the expected benefit. Pushing in the other direction is the need to reduce $\hat{T}_{e,d}$ by increasing the parallel connection length (a rather weak function). This would also provide increased screening from sputtered impurities or recycled neutrals, which might be beneficial to confinement. However, there is not much experimental evidence for this effect. Therefore, we have chosen $L_{\perp,d} \simeq 15$ cm largely as the result of magnetic equilibrium considerations and confirmed it by B2 calculations that show an acceptable trade-off between $\hat{q}_d$ and $\hat{T}_{e,d}$. The parallel connection length from outboard midplane to the divertor plates is about 20 m.

At the divertor, the magnetic flux surfaces intersect the target plates at nearly normal incidence, as shown in Fig. 9.1. The solid lines correspond to the start of the X-point sweep, while the dashed correspond to the end of the sweep. The magnetic flux expansion from midplane to the divertor ranges from 14:1 to nearly 20:1 at the end of the sweep. A single sweep is planned; multiple sweep capability will be provided by the coil set. Significant performance is gained by multiple sweeps, but only in the case that the power scrape-off width is narrower than predicted below. Figure 9.2 shows two possible sweep programs and the resulting peak surface temperature at the targets; the optimized sweep adjusts the programmed motion

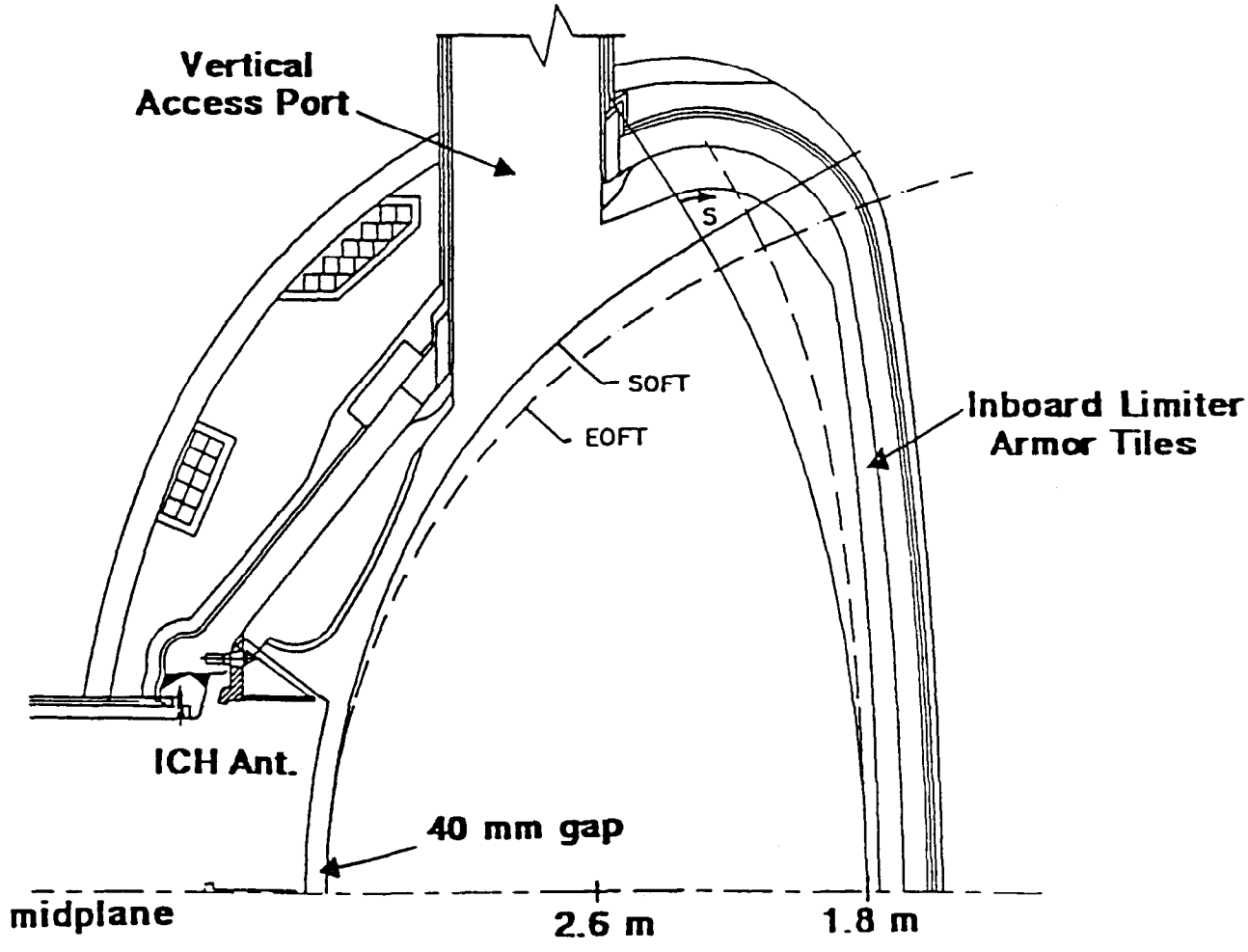

Fig. 9.1. Cross section of the BPX upper divertor region, showing the separatrix flux surface at the beginning and end of the X–point sweep.

to minimize the surface temperature rise.

The magnetic field lines at the strike-points are nearly tangent to the divertor targets, having an angle of incidence θ_B of about 1.3 deg. This shallow angle forces strong constraints on the alignment of the divertor tiles since the heat flux on an exposed edge is $1/\sin\theta_B$ or $\simeq 40$ times that on the flat surfaces of the divertor tiles.[9] A toroidal sawtooth pattern has been proposed (see Sec. IX.E) for the divertor tiles to minimize this potential problem. This pattern will have to be matched to the field helicity and to the ripple in the toroidal field to minimize heat flux peaking due to the modulation of the angle of incidence ($B_{T,max}/B_{T,min} \simeq 1.01$ at the outer strike-point).

Away from the divertor, the minimum clearance between the separatrix flux surface and the inner wall or ICRF antenna shields is planned to be large enough so that recycling from those surfaces will not be a problem. This means separations of the order $2 \times \lambda_n$, the density e–folding length at the midplane. Currently, the minimum gap is 4 cm from the ICRF antenna Faraday shield to the separatrix at the outboard midplane, which compares with 1.3 to 2.6 cm for λ_n predicted from B2 simulations.

IX.C. DIVERTOR OPERATION

Central to the BPX design is the idea that it will operate with H-mode confinement to achieve the required fusion performance. H-mode operation has numerous implications for the divertor design, some of which are: the SOL density will be lower and its width reduced compared to L-mode operation (yielding lower neutral and impurity screening), the power distribution among the strike-points may be changed, and edge-localized

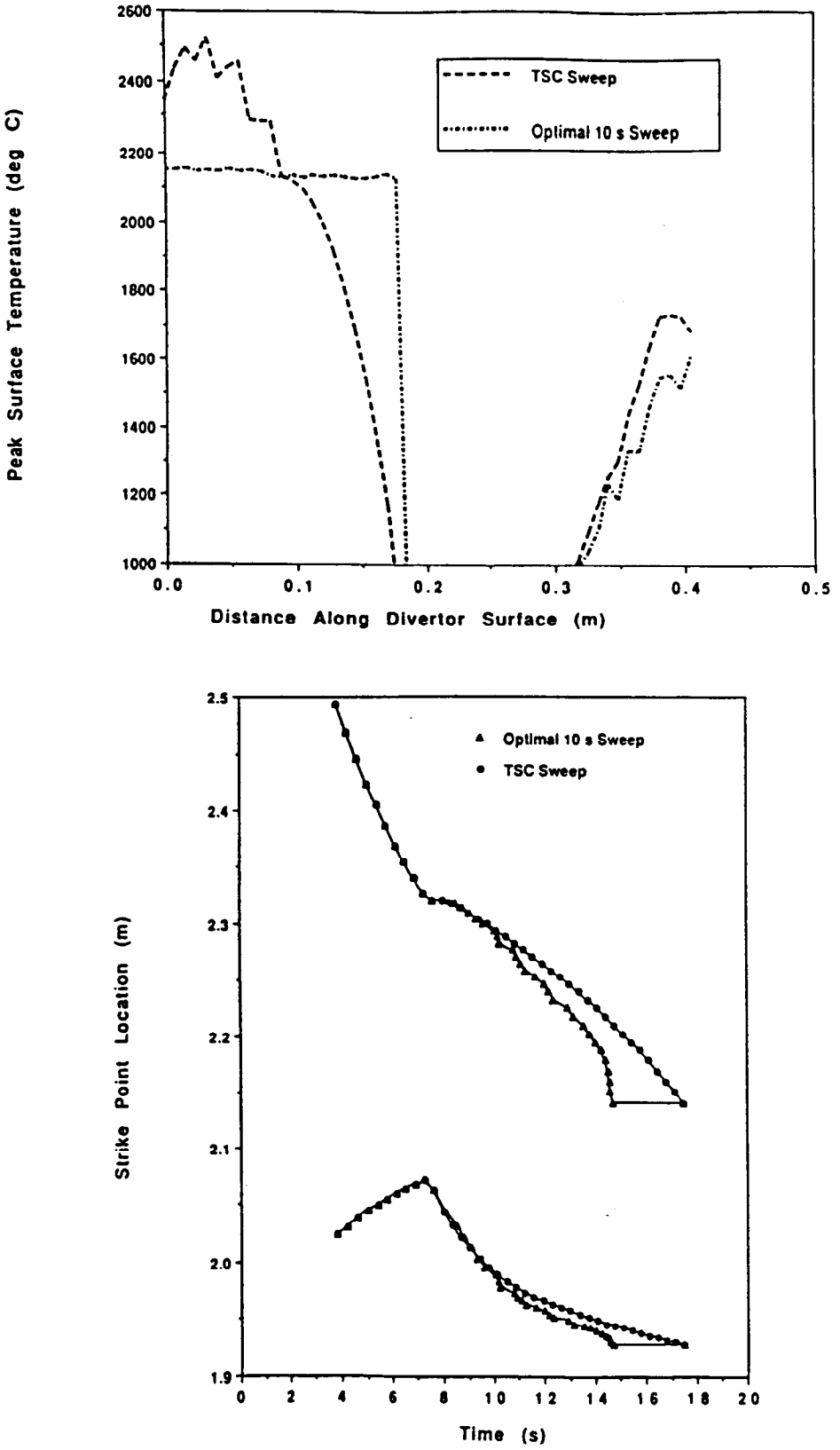

Fig. 9.2. Possible divertor sweeping programs: (a) the resulting peak surface temperatures and (b) the radial position of strike-points versus time.

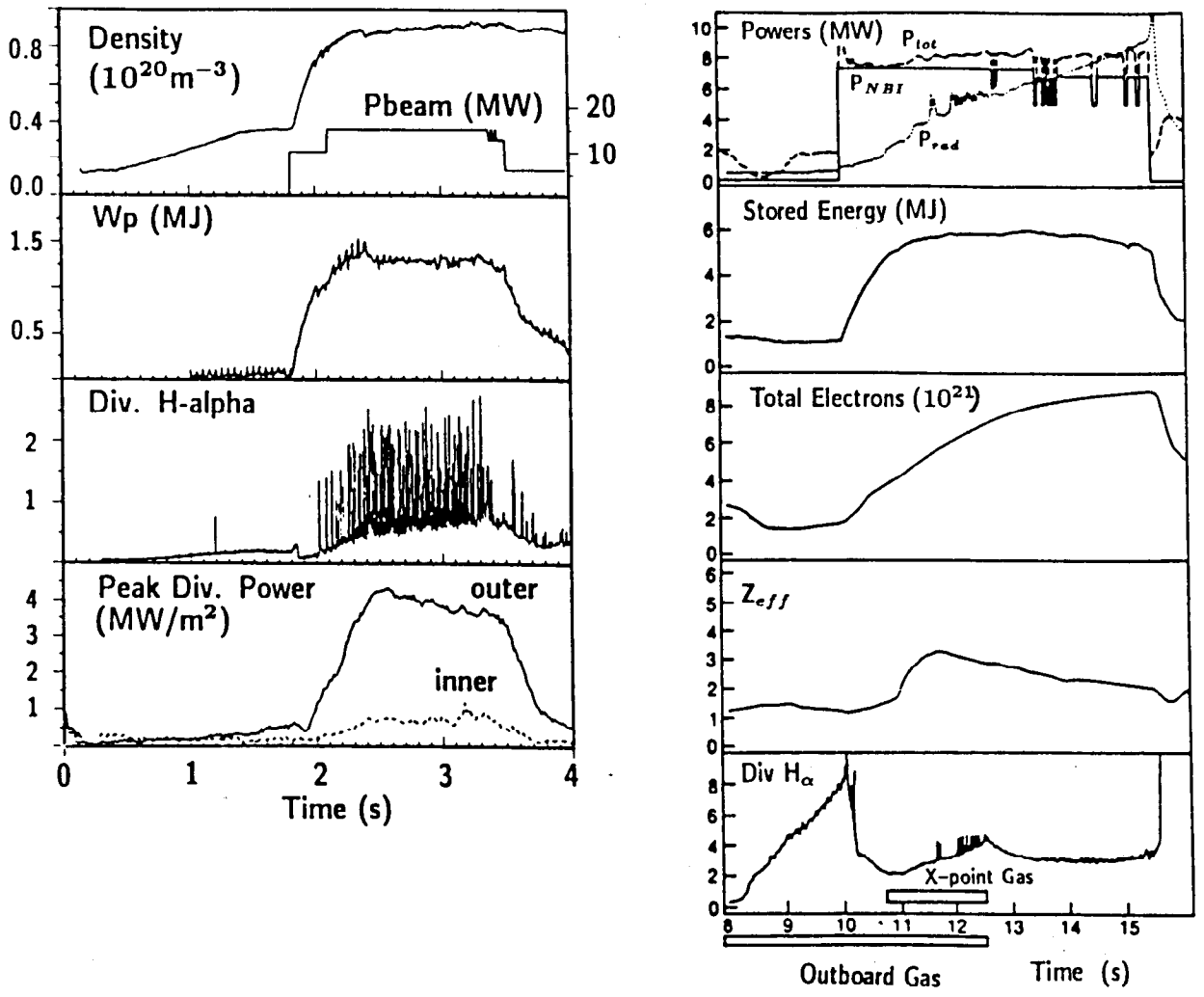

Fig. 9.3. Representative H-mode discharges[3,11] from DIII–D(left) and JET (right). In the case of JET, divertor gas injection delays the onset of carbon blooms.

modes (ELMs) may produce large heat pulses on the divertor plates. Therefore, in this discussion we concentrate on the divertor parameters for H mode, especially since an L-mode discharge will likely operate at significantly lower power levels. The probability of achieving H mode in BPX is discussed in more detail elsewhere in this paper. We note here only that the threshold power for a single-null divertor configuration with the ion ∇B drift in the direction of the X-point is somewhat lower than that for the double-null. The threshold is approximately 50% higher than the SN case for inner wall–limited discharges, as reported by the DIII–D and JFT–2M groups.[8,10]

IX.C.1. ELMs and H Mode

It is important to first distinguish between the two types of H-mode discharge: ELM–free quiescent and ELMing H modes. Representative time histories for each type[3,11] appear in Fig. 9.3 (from JET and DIII-D). Note that the ELMing H mode does have an initial ELM–free period during which the density rises. In all cases, this density rise occurs without external fueling and is thought to be the result of a sudden rise in particle confinement time coupled with a sustained flux–independent particle release from the walls.[12] This effect may be relatively less prominent in BPX with its high operating density, but τ_E and τ_p are comparable to JET's.

ELM–free quiescent H modes are characterized by a steady buildup of plasma density, temperature, and impurity radiation.[13] In some cases, hollow profiles have been observed during this buildup.[14] Usually, the quiescent period is terminated by the start of ELM activity, which reduces

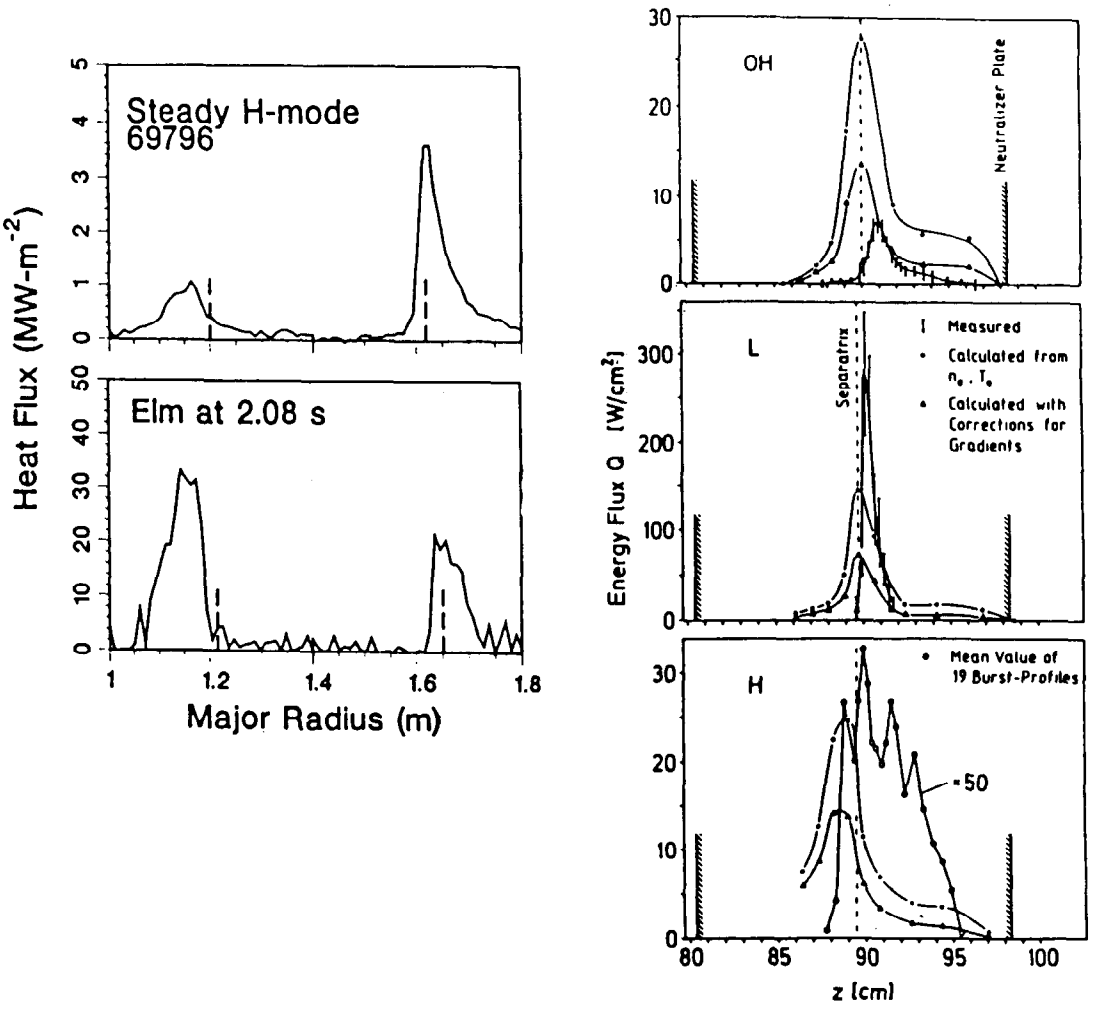

Fig. 9.4. Divertor heat flux profiles from DIII–D (left) and ASDEX (right), showing the effect of ELMs. The ASDEX data[22] are for the outside strike-point only; the DIII–D data[21] show both.

the density and impurity content of the plasma. If the heating pulse lasts long enough and no ELMs occur, the radiative losses grow to nearly equal the input power, and H-mode confinement is lost; this is typical of JET plasmas.[15] Truly steady-state ELM–free H-mode discharges have not been observed.

ELMing H modes can achieve quasi-stationary conditions due to periodic losses from the plasma edge.[16] These tend to clamp the line–average density and the buildup of impurity radiation from the core. It is currently thought that ELM behavior may be explained in terms of ideal ballooning mode theory[17,18]: ELMs occur when the edge pressure gradient exceeds a threshold value that depends on the magnetic shear near the edge. Higher heating power drives the pressure up faster and makes more ELMs, while higher B_T and I_p raise the stability limit and so lower the ELM frequency.

In spite of the many observations supporting these general trends in ELM behavior, predicting whether or not BPX will have ELMing H modes is not straightforward. Generalized profile comparisons (e.g., the same normalized volume–averaged beta implies the same ELM behavior) are not sufficient since the key physics is at the *edge*, where the mechanisms determining the scale length (dp/dr) are not well understood. Thus, small shaping changes, which affect only the edge magnetic shear and not the overall beta limit, can dramatically affect the ELM behavior.[18] For plasmas with similar edge stability limits, the radial energy flux across the edge plasma is a big factor in determining the level of ELM activity.[16] The lack of ELMs in JET is consistent with this picture since it has a much lower energy flux across the separatrix than either ASDEX or DIII–D, as shown in Table 9.1. Similarly, we might expect to see ELMing H modes in BPX at full power since its power density at the edge will be high. The frequency of the ELMs will

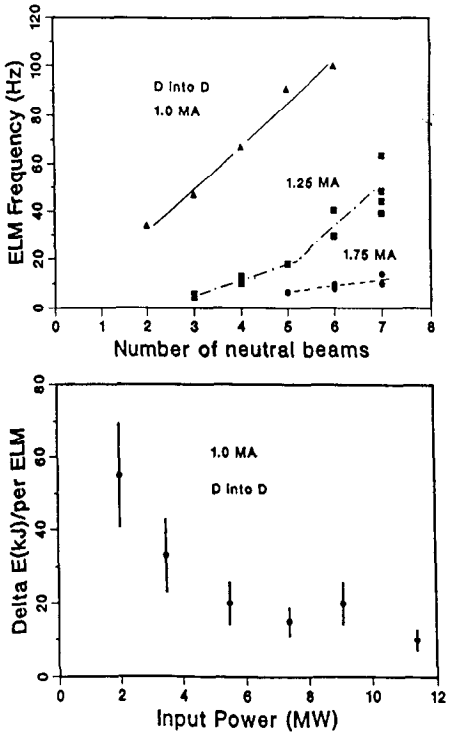

Fig. 9.5. Frequency and amplitude of ELMs in DIII–D as a function of plasma current and input power.[23]

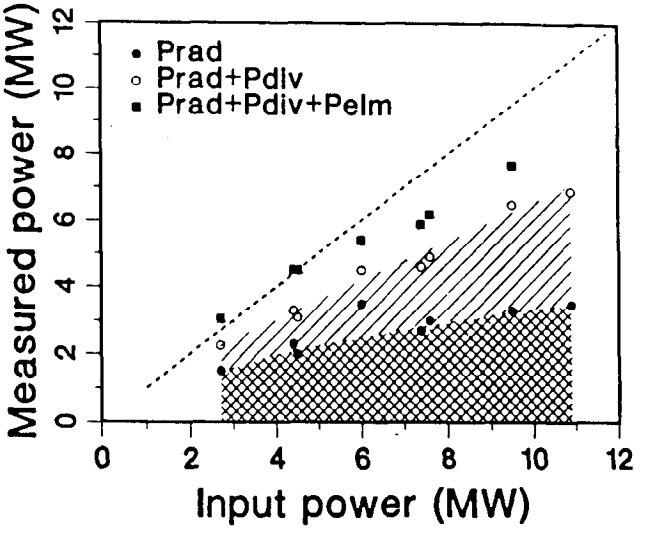

Fig. 9.6. Global power balance[3] for ELMing H-mode discharges in DIII–D: P_{elm} is the time-averaged power deposited by ELMs, and P_{rad} is the total radiative loss. Here, $I_p = 2$ MA, $B_T = 2.1$ T, $Z_{eff} \simeq 1.6$ to 2.0, and neutral deuterium is being injected into a deuterium plasma.

probably grow during the discharge as the fusion power rises.

The significance of ELMs to the plasma boundary lies in the fact that they produce large power bursts at the divertor targets and broaden the SOL significantly.[19] This broadening has been observed both at the divertor and at the plasma midplane, where its effect on ICRF coupling has been documented.[20] Divertor heat flux profiles due to large ELMs in ASDEX and DIII–D are reproduced here[21,22] as Fig. 9.4. The peak values are up to 20 times larger than the time-averaged value between the ELMs. Fortunately, the ELM amplitude is observed to drop sharply as their frequency rises,[23] as shown in the DIII–D data of Fig. 9.5. Individual ELMs in high-power discharges may remove only 1% of the total stored energy. There is at present no predictive model for this behavior.

Based on observed ELM behavior, we expect that ELMs will not be catastrophic for the BPX divertor in a nearly ignited plasma. Given a total stored energy of 90 MJ at full power and assuming a 2% loss per ELM spread out over twice the usual divertor contact area with a 2-ms duration, we find that the transient surface temperature rise for pyrolytic graphite would be about 600° C. This would result in sublimation of a thin surface layer from the tiles (already hot from the steady-state heat flux). How much of this carbon would escape the divertor region, as opposed to being redeposited, depends on the plasma conditions in front of the target plates following the ELM. Recent measurements from ASDEX suggest[24] that ELMs can more than double the time–averaged sputtering rate of the divertor material (copper in their case). In both ASDEX and DIII–D, ELMs deposit more energy at the cooler inner divertor strike-point than at the outer.

IX.C.2. Power Balance and SOL Heat Flux Distribution

Global power balance measurements for quiescent H-mode plasmas have been reported from a number of devices.[22,25–27] The total power reaching the divertor is generally less than 40% of the input power. The remainder of the power goes into radiative losses (30 to 60% – growing with time after the H-mode transition) and into building up the stored energy. A significant fraction of the power losses (~20%) usually remain unmeasured. In ELMing plasmas, the contribution of the ELM-induced energy loss to the overall power balance has been determined in both ASDEX and in DIII–D. ASDEX reports[24] that there is a 50/50 power split between the ELM and quiescent-phase losses, whereas a steady decrease in this ratio with increasing heating power is reported[3] for DIII–D. These results appear in Fig. 9.6.

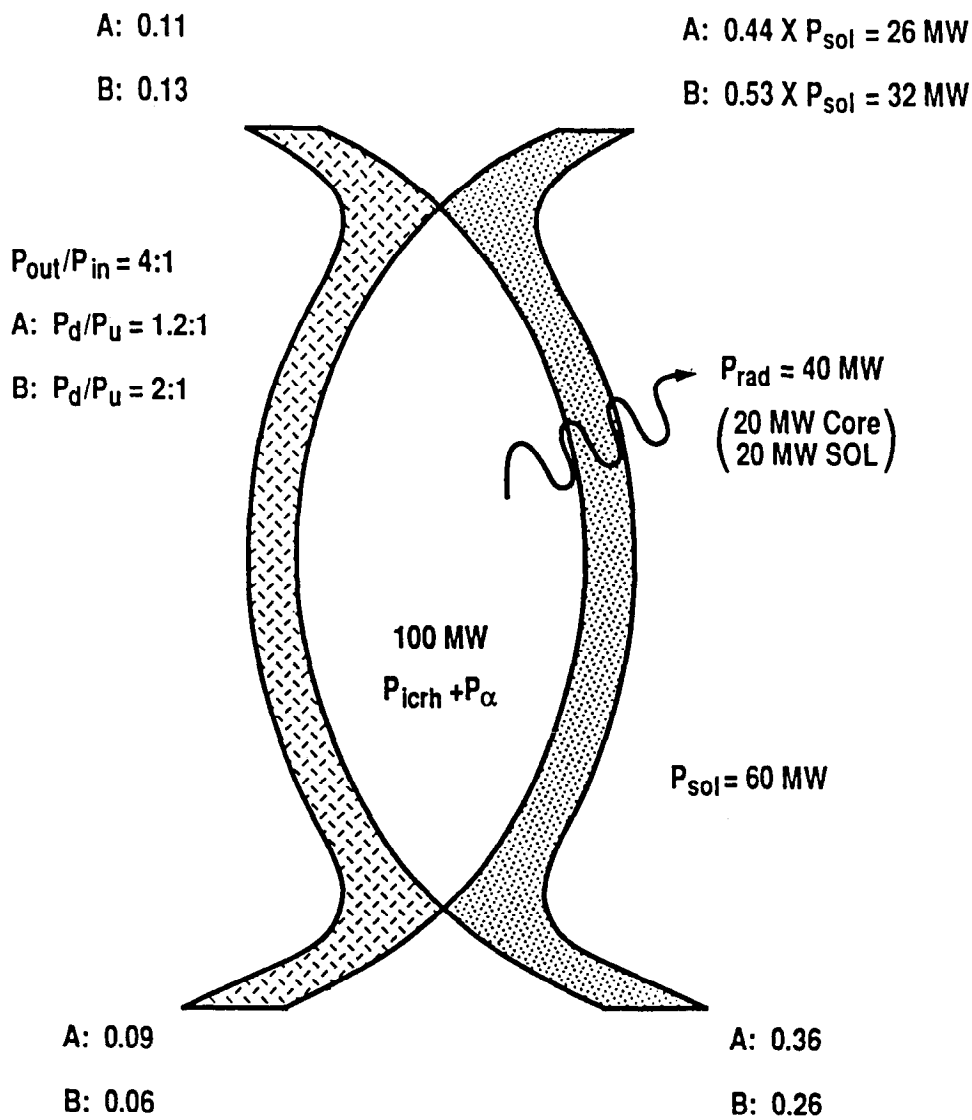

Fig. 9.7. Distribution of energy losses assumed for BPX divertor studies.

Figure 9.7 illustrates the assumptions about the H-mode power balance and heat flux distribution used for the BPX reference discharge with $P_{loss} = P_{heat} = P_{ICH} + P_{\alpha} = 100$ MW. We assume that 40% of the total input power P_{heat} is radiated as follows: 20% as bremsstrahlung and cyclotron radiation from the core [from typical Tokamak Simulation Code (TSC) modeling with $Z_{eff} = 1.65$], 10% as impurity radiation from the edge and SOL plasma, and 10% as localized radiation in the divertor region. We thus work with the assumption that 60% of the heating power is conducted in the SOL plasma. As described below, numerical simulations predict that hydrogen line radiation in the divertor will reduce this by another 6%, so that 54% of the total heating power should actually reach the divertor plate (including 13.6-eV recombination energy). This figure is matched experimentally only in low-density L-mode discharges.[2] However, with relatively higher density (lower Z_{eff}), and certainly higher temperatures and all-carbon walls, a lower radiative loss fraction may be expected in BPX, so 54% may not be overly conservative. A better estimate of the radiative losses awaits new models of SOL impurity behavior, as discussed below.

Published data on the divertor heat flux distribution for double-null divertor tokamaks[3,24,25] show that about 80% of the total divertor power is deposited at the outer targets. The up-down symmetry of the power distribution is sensitive to the positioning of the X-points. Measurements in ASDEX and DIII-D show[3,24] that effectively single-null operation is obtained if the flux surfaces tied to each null are not positioned to within λ_q of each other at the midplane. Even with excellent magnetic balancing, however, there are indications that

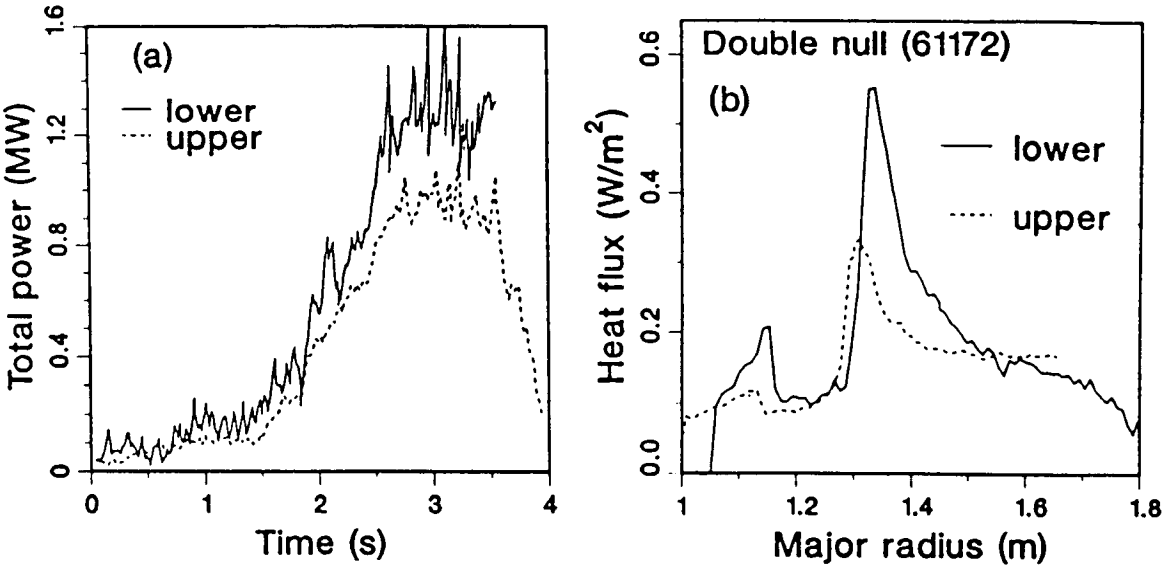

Fig. 9.8. Divertor heat flux[3] for DN discharge in DIII–D: (a) Total integrated divertor power and (b) radial heat flux profiles at 2.8 s.

the peak heat flux is greater to the divertor in the ion ∇B drift direction. Figure 9.8 shows such up-down asymmetries in the peak (2:1) and the total (1.2:1) divertor heat flux for a DN discharge in DIII–D for which the magnetic flux surfaces for each null were maintained to within less than $0.5\lambda_q$ during an ELMing H mode. However, no attempt was made to adjust the magnetics to achieve better heat-flux balance. It is thought that this asymmetry results from E×B drift effects in the SOL transport. We include the numbers for both asymmetries in Fig. 9.3: 26 MW to one quadrant for 1.2:1 (A), and 32 MW for the 2:1 case (B).

IX.C.3. Edge Density and Temperature

It is important to have some idea of what the electron density on the separatrix will be in BPX because it significantly impacts the predictions for the peak electron temperature at the divertor target and, to some extent, the peak divertor heat flux. High edge density near the midplane will yield a high-density, low-temperature plasma at the divertor plates. H-mode operation means relatively flat density profiles with a steep density gradient at the edge. Pellet fueling of H-mode plasmas may peak the central density by adding particles to the core, but it leaves the edge density pedestal relatively intact. Experimental data[28,29] suggest that $n_{e,sep}/\hat{n}_e \simeq 0.2$ to 0.4, with considerable uncertainty arising from lack of a precise determination of the separatrix position. Furthermore, these data suggest that the ratio may drop with time following the H-mode transition. The ITER design team uses 0.28 as a reference value for this ratio.[30] We have nominally chosen 0.25, which then yields $n_{e,sep} = 1 \times 10^{20}$ m^{-3} for $\hat{n}_e = 4 \times 10^{20}$ m^{-3}. This operating point is about three to five times higher than that obtained in JET or DIII–D. More measurements here are needed.

Centrally peaked electron temperature profiles are expected in BPX H-mode plasmas. We do not, as yet, have a firm idea of $T_{e,sep}$. Where detailed edge measurements are available, the data at first seem conflicting. ASDEX and PDX report[31,32] a strong increase in electron temperature near the separatrix following the H-mode transition, whereas only a modest increase is observed[17] in DIII–D. It has been suggested, based on more recent ASDEX operation with a new divertor configuration, that the larger $T_{e,sep}$ pedestal may be associated with a more closed divertor geometry. The actual value that will be obtained depends on details of the radial energy transport near the edge in a self-consistent way: It is assumed that $q_{sep} \propto n\chi\nabla T$. Unfortunately, there is as yet no clear picture of the loss mechanisms across the separatrix of H-mode plasmas. For many of the SOL simulations described below, we have fixed the edge density and total heat flux out of the core, then calculated the $T_{e,sep}$ and $T_{i,sep}$ consistent with assumed energy transport coefficients. The resulting temperatures are in the 200- to 700-eV range. Since BPX will operate at high density,

it is tempting to think that $T_i = T_e$ near the separatrix, but the SOL plasma near the separatrix is only marginally collisional due to the relative short connection length to the divertor targets and the high temperatures near the midplane ($L_\parallel/\lambda_{ei} \simeq 1$ to 5 for $Z_{eff} = 1$ in the SOL). Recent data from JET points to $T_i > T_e$ near the separatrix for high-power discharges.[33] The impact of ICRF on the velocity distributions in the edge plasma is not known.

IX.D. BASIC PHYSICS OF THE SOL PLASMA

In this section, we examine the essential elements of the particle and power flow in the edge plasma. The purpose of these "back-of-the-envelope" calculations is to obtain a rough estimate (within factors of 2 to 3) of the divertor parameters and their scaling to guide our intuition when working with the more complete two-dimensional multifluid numerical simulations. A number of two-point or one-dimensional models of the SOL plasma have been developed for this purpose.[34,35] The two most common features of these models are the following assumptions:

1. Energy transmission is across a collisionless sheath at the material wall, with a sheath transmission factor of $\gamma \simeq 7$ to 8, where γ is defined as $q_d = \gamma n_e T_e C_s$.
2. Classical particle and energy transport along field lines (Spitzer thermal conductivity) is balanced by anomalous cross-field transport (characterized by χ and $D_\perp$).

In general, these simple models match the measured qualitative behavior of the divertor plasma pretty well.[36] Additional physics concerning particle recycling at the limiter/divertor surfaces, and/or impurity radiation in the SOL, has been included by several authors.[37]

IX.D.1. Heat Flux Profiles

Under conditions where the sheath dominates the energy flux, Harbour[38] and Harrison[39] arrive at the following expression for the heat flux e-folding length at the plasma midplane:

$$\lambda_q \simeq \left[\frac{\chi_e L_\parallel}{0.5\gamma C_{s,d}}\right]^{\frac{1}{2}}, \qquad (9.1)$$

where $L_\parallel$ is the parallel connection length (flux-surface averaged midplane to divertor), γ the sheath energy transmission coefficient, and $C_{s,d}$ the ion sound speed at the divertor target, equal to $10^4\sqrt{T(\mathrm{eV})}$ m/s for deuterium. So in this case, the radial e-folding length for the heat flux at the midplane depends on χ but is nearly independent of the energy flux into the SOL (a slight variation appears through the sound speed).

In the other extreme, when the parallel thermal conductivity of the SOL plasma is the limiting factor, Harrison shows that $\lambda_q \propto (\chi_e/q_{sep})^{1/2}$, where q_{sep} is the power density across the separatrix. In this case, because the parallel thermal conductivity rises with temperature, the width of the scrape-off layer decreases with power and the peak divertor heat flux varies as $P^{3/2}$ instead of linearly with P, as above. Such behavior has been predicted from B2 modeling for the NET/INTOR divertor. As shown below, we see something more like the linear behavior in the B2 modeling for BPX.

Once the width of the profile is known, the peak divertor heat flux follows immediately using the magnetic flux expansion at the target, the total energy loss into the SOL, and the distribution of the power among the four divertor strike-points. Thus,

$$\hat{q}_d = \frac{P_{quad}}{2\pi R \times 0.8\lambda_{q,d}}, \qquad (9.2)$$

where P_{quad} is the total power to one quadrant of the the SOL, R is the major radius, and $\lambda_{q,d}$ the e-folding length mapped to the divertor target with 0.8 resulting from the integral over a cut-off exponential profile. For BPX with $P_{quad} =$ 26 MW, $T \simeq 50$ eV at the target, $L_\parallel \simeq 20$ m, and $\chi_e = 2$ m^2/s, we obtain $\lambda_q = 1.2$ cm at the midplane using Eq. (9.1). Combining this result with the 14:1 magnetic flux expansion and 1.2:1 up-down asymmetry outlined in Sec. IX.C.2 yields an estimated peak divertor heat flux of 13 MW/m^2 (16 MW/m^2 for the 2:1 up-down asymmetric case). For comparison, the B2 simulations described below yield $\lambda_q \simeq 0.5$ cm and a peak divertor heat flux of $\sim$20 MW/m^2 for these same plasma conditions (see Table 9.2).

It is clear that choosing the correct value for χ_e is central to predicting the width and peak of the divertor heat flux profile in BPX. Data from present divertor experiments with $B_T = 1$ to 4 T is consistent[30] with χ ranging from 1 to 4 m^2/s, the lower values corresponding to ELM-free H-mode discharges. While Stangeby and McCracken[40] report measurements of the B_T scaling for λ_n and λ_T in limiter plasmas, no similar measurements for the heat flux profile in either L-mode or H-mode divertor plasmas have been reported. If we take the lowest published χ_e (1 m^2/s from DIII-D) and scale it like T_{sep}/B, then $\chi_e \simeq 0.8$ m^2/s is obtained,

Table 9.2. Input Parameters for B2 Simulations

Quantity	Value (Ref. Case)	Range
$n_{e,sep}$ (m^{-3})	10^{20}	0.4–1.5
$T_{e,sep}$ (eV)	350	300–700
Q_{sep} (MW) (1 quadrant)	26	7–57
P_e/Pi	1:1	1:1–3:1
χ_e (m^2/s)	2.0	1–3
χ_i (m^2/s)	0.6	0.3–1.0
$D_\perp$ (m^2/s)	0.6	0.3–1.0
v_{conv} (m/s)	-20	-20 to 0
R_{div}	0.97	0.90–1.0
Flux limiter	0.2	0.1–0.2

and the analytically estimated λ_q would drop to 0.6 cm.

IX.D.2. SOL Density and Temperature Profiles

A similar estimate for the density profile e-folding can be obtained by balancing parallel and perpendicular particle transport. Stangeby and McCracken's study of the variation of λ_n with toroidal field for a number of limiter and L-mode tokamaks concluded that the data were consistent with Bohm-like cross-field transport. That is,

$$\lambda_n \propto \sqrt{\frac{L_\parallel D_B}{v_{flow}}}, \qquad (9.3)$$

where $D_B = 0.06T[\text{eV}]/B[\text{T}]$ and v_{flow} is the average flow speed from the midplane to the limiter or divertor (which is ~0.1 to 0.3 times the local ion sound speed). These data appear in Fig. 9.9, with the region applicable to BPX corresponding to $\lambda_n \simeq 1$ to 2 cm and $D_B \simeq 1.5$ m^2/s. Analysis of scrape-off layer density measurements for H-mode discharges in DIII-D and ASDEX yield diffusion coefficients that are of the same order as the Bohm values[29,41] (~0.5 to 1.0 D_B), but there is no mention of their B_T scaling. In the far SOL of H-mode plasmas (more than 1 to 2 × λ_n), the density falls off much more slowly than near the separatrix, suggesting a larger $D_\perp$. This clearly disagrees with Bohm scaling. Neuhauser et al. speculate that this plateau is associated with increased plasma fluctuations.[41]

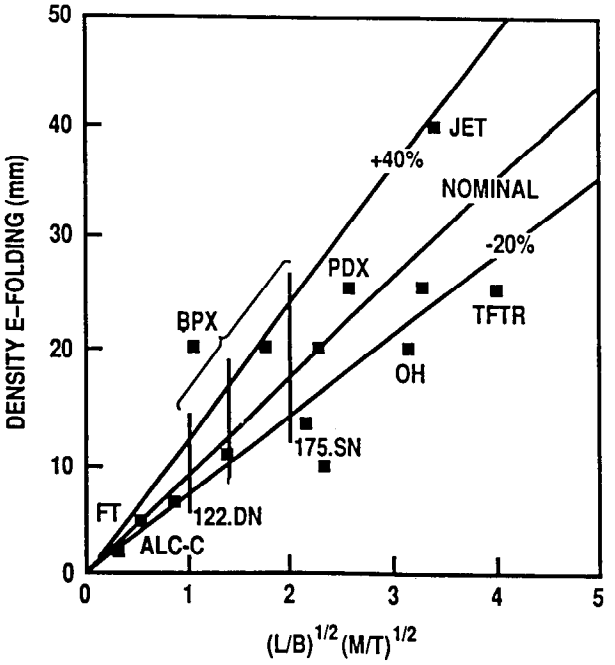

Fig. 9.9. Scaling of SOL density radial e-folding length versus normalized parallel connection length for several tokamaks.[40]

The peak electron temperature at the divertor cannot be estimated analytically as simply as the divertor heat flux. This is because it depends on the local recycling coefficient at the divertor plate, for which there is no simple formula. This relationship is illustrated in Fig. 9.10, which is adapted from Post, Langer, and Petravic.[42] It shows $T_{e,d}$ as a function of the energy loss per ion across the separatrix. $T_{e,d}$ is derived from the ion flux and the energy transmission coefficient of the sheath, assuming no energy loss in the SOL from radiative processes. The ion flux at the divertor is $R = 1/(1-r)$ times the flux across the separatrix Γ_{sep}, where r is the local recycling coefficient and R is Post's flux amplification factor. The shaded regions indicate the operating range for several tokamaks using published values[29,43] for $T_{e,d}$. It is clear that a high recycling coefficient is needed to keep $T_{e,d}$ low and to minimize sputtering. Obtaining a good estimate of r is difficult because it is sensitive to the surface conditioning of the divertor targets and to the probability that recycled neutrals can escape without reionization. Similarly, $\Gamma_{sep} = N_p/\tau_p$ is not well known. We currently rely on DEGAS neutral transport calculations[44] to determine r and the WHIST core-plasma transport code[45] to determine Γ_{sep}.

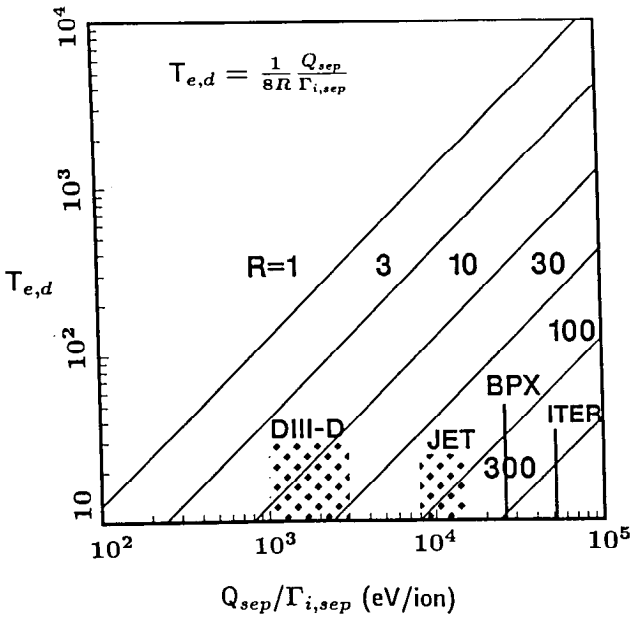

Fig. 9.10. Relationship between peak divertor electon temperature and the energy loss across the separatrix and divertor recycling coefficient, according to Ref. 42.

IX.E. NUMERICAL SIMULATION OF THE SOL PLASMA

Simple models alone do not suffice for choosing the operating point of the BPX divertor because details of the radial profile shape can have severe consequences for the engineering design. For example, the peak divertor heat flux could differ by a factor of 2 between assuming a simple one-sided exponential and using a full Gaussian profile consistent with radial transport into the private region below the X–point. Therefore, we are modeling the SOL and divertor plasma using the fully two–dimensional Braams B2 code, which was originally developed as part of the NET program. B2 is now the most widely used edge plasma model in the United States and forms the basis of predictions of the operating point for the ITER divertor. As described in Sec. IX.E.2 below, it has been successfully validated against experimental data on ASDEX, DIII–D, and TFTR, though this work is still continuing. Work on other two-dimensional codes is also being carried out.[46]

IX.E.1. The B2 Code

The B2 code simulates the SOL plasma by solving the fluid equations for particle, energy, and momentum balance on a two-dimensional rectangular mesh. This mesh is mapped to the actual SOL magnetic geometry using a prescribed set of metric coefficients derived from MHD equilibrium calculations. Figure 9.11 shows the typical mesh (24 radial by 32 axial points) used to model the lower half of the outside SOL of BPX. The mesh extends from slightly inside the separatrix (necessary to include the so–called "private region" between the strike-points) to 4 cm outside at the midplane, and it has nonuniform cell size to account for the steep spatial gradients near the separatrix and the strike-point (where the cells are about 0.5 × 0.5 cm). It is assumed that the wall of the tokamak smoothly matches the outermost flux surface, so the effect of localized ICRF antenna shields is neglected. A detailed description of the physics and numerical analysis used in B2 has been prepared by Braams.[4]

To complete a B2 run, boundary conditions and transport coefficients must be selected. The radial transport coefficients $D_\perp$, $\chi_{i,e}$, and v_{conv} act uniformly over the mesh and are all anomalous (i.e., set by the user — usually to values that have been determined from comparison with existing tokamak data). Classical parallel energy transport (i.e., Spitzer conductivity plus convection) is assumed, with the inclusion of an electron heat flux limiter of 0.1 to $0.2v_e$ for low collisionality $(e-e)$ conditions. The value of the flux limiter is based on simulation results from fully kinetic one-dimensional models.[47] Other assumptions used in the simulations include zero parallel momentum input at the midplane, a specified particle recycling coefficient at the divertor plate, zero flux to the outer wall, and a currentless sheath condition at the divertor target. Two combinations of boundary conditions along the separatrix have been used: fixed density and temperature (leaving the energy and particle fluxes to be calculated) or fixed density and radial heat flux (leaving the particle flux and electron temperature along the separatrix to be determined). There is no significant difference between the results from these two operating modes. Table 9.2 lists the input values used in the reference case B2 runs made for this study; the range over which these were varied is also shown.

We mention here that the assumption of a currentless SOL is not correct since net current flow in the SOL plasma has been measured.[43,48] It is thought that this current is driven by thermoelectric forces arising from poloidally nonuniform energy flow across the separatrix.[49] It is predicted that these forces and currents can have a significant effect on the divertor heat flux distribution,[50,51] so we are upgrading the B2 code include them. Preliminary results[52] show that up-down heat flux asymmetries do result, similar to those measured in DN discharges.

We have not included the effects of impurities explicitly in the B2 calculations for BPX because of

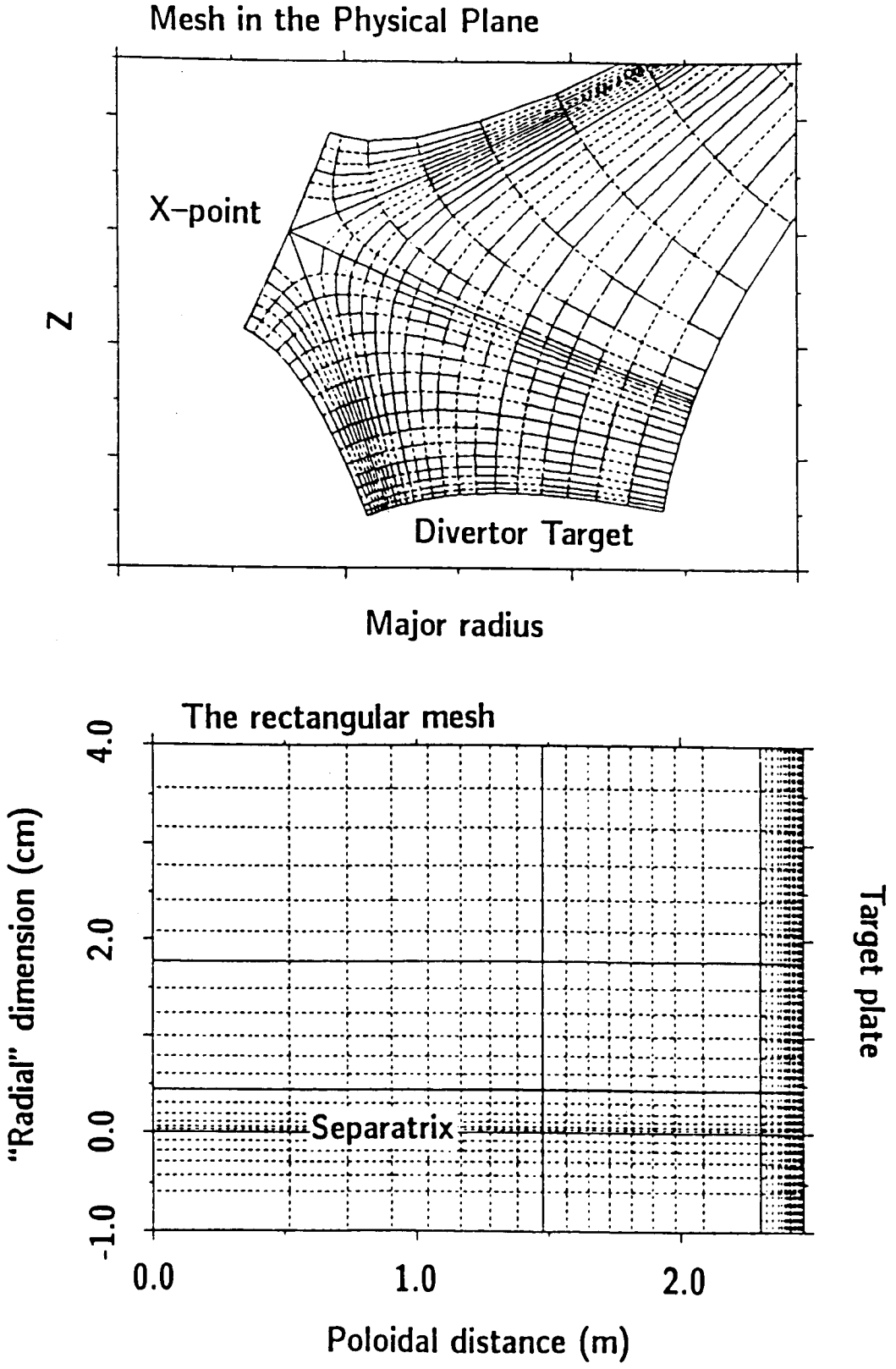

Fig. 9.11. Mesh geometry used in the B2 simulation of the BPX SOL plasma.

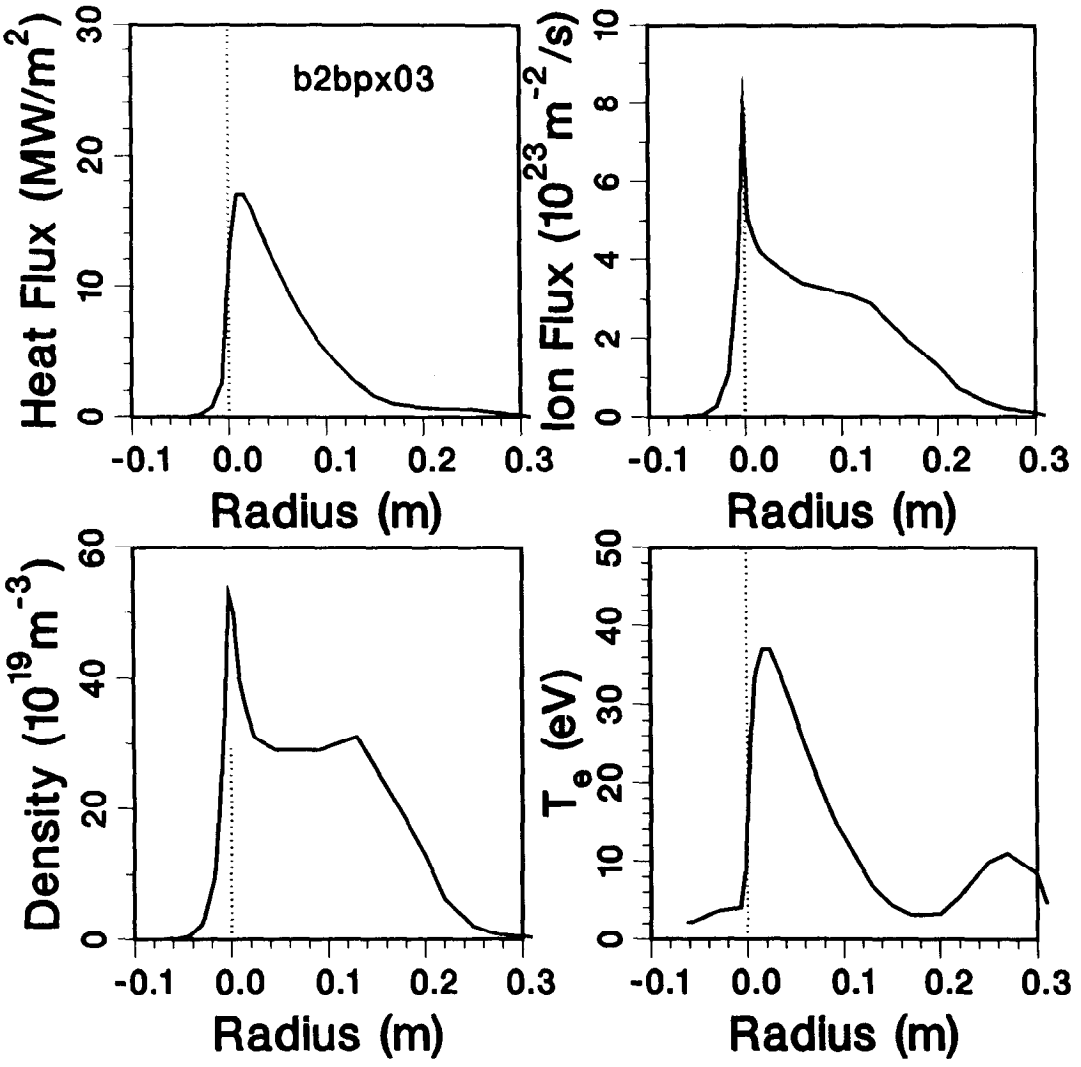

Fig. 9.12. B2 simulation of the divertor profiles for the BPX 500-MW reference plasma (B2 run b2bpx03). (a) heat flux; (b) electron density; (c) ion flux, with chain-dot corresponding to zero wall recycling; and (d) electron (solid) and ion (dashed) temperature. Vertical dotted line denotes the separatrix.

difficulties in obtaining convergent solutions with more than two-fluid interactions. Carbon radiation from the SOL and divertor plasmas should be significant at the concentrations expected (based on DIII–D data, we expect $Z_{eff,SOL} > Z_{eff,core}$). However, it is difficult to make "back-of-the-envelope" calculations of impurity radiation in the SOL because the radiative efficiency for each charge state is a very sensitive function of the impurity ion lifetime. As a first approximation to accounting for finite carbon concentration, we have reduced the total energy flow into the SOL, $P_{SOL} = \int_{sep} q_{sep} dA$, by an amount consistent with global power balance measurements in existing tokamaks, as discussed in Sec. IX.C.2. B2 then calculates only the hydrogenic losses in the SOL plasma (~6% of P_{SOL} excluding charge-exchange). That is, we let $P_{SOL} = 60$ MW for the input to the B2 runs, instead of 70 MW. We also leave $Z_{eff} = 1$ in the SOL for the B2 runs, which errs on the conservative side, since larger Z_{eff} results in reduced parallel thermal conductivity and a lower peak heat flux. Work is now under way to develop SOL models that can handle finite impurity concentrations, starting with one-dimensional codes[53] to reduce the numerical difficulties and to avoid using a set of arbitrary radial transport coefficients about which there is no experimental data.

IX.E.2. B2 Simulation Results

In this section, we present results from B2 modeling for the reference case plasma with $P_{heat} = 100$ MW and $P_{quad} = 26$ MW, which refines the

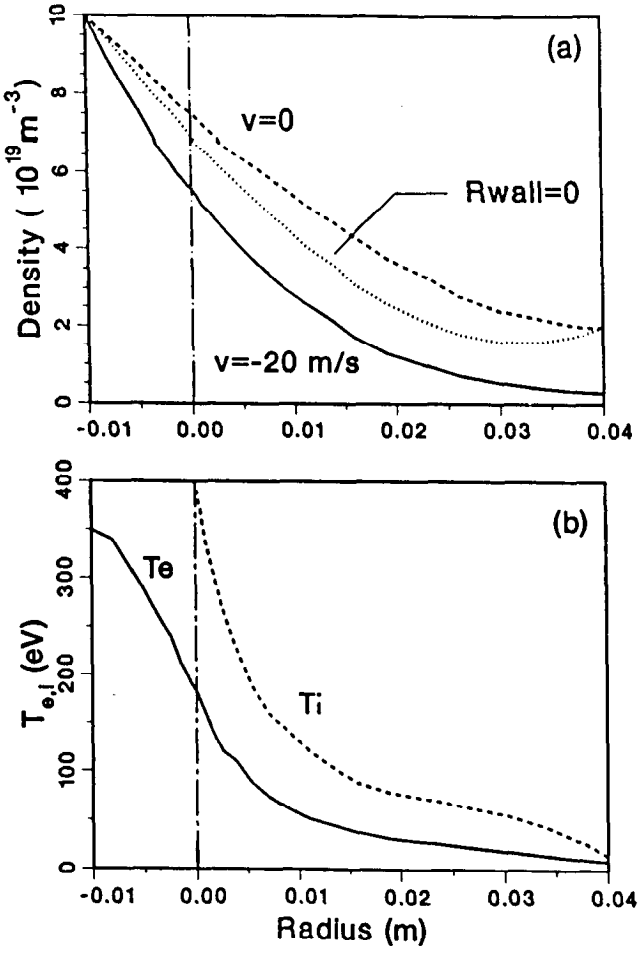

Fig. 9.13. B2 simulation of the midplane profiles for the BPX 500-MW reference plasma (B2 run b2cit87): (a) electron density; and (b) ion and electron temperatures. Chain-dot line denotes the separatrix.

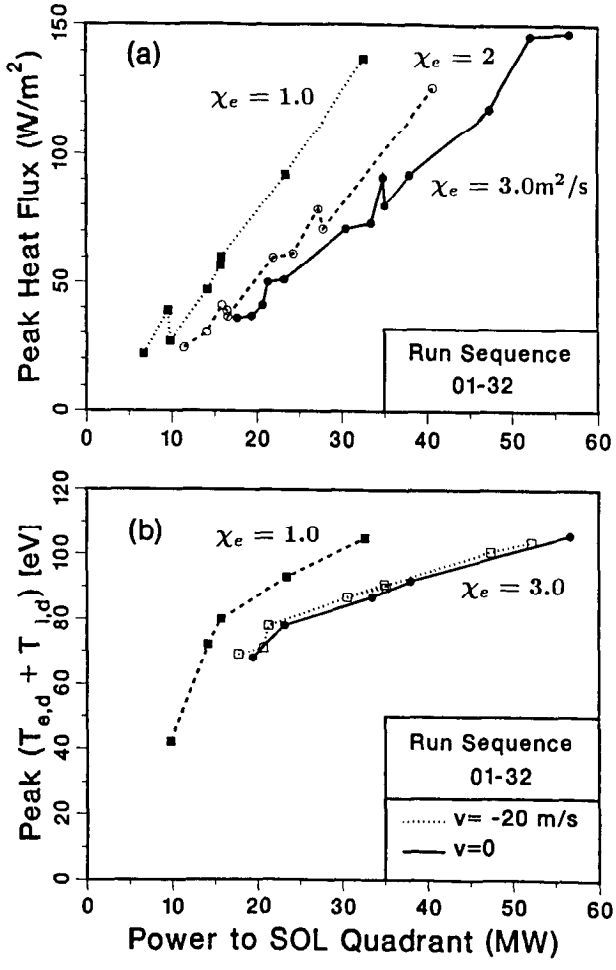

Fig. 9.14. Variation of peak divertor heat flux and plasma temperature with radial transport coefficient χ and inward convection term.

simpler estimates presented earlier. Profiles at the outer divertor plate appear in Fig. 9.12. The peak heat flux reaches 17 MW/m^2 with a $1/e$ width of 6 cm. This maps back to $\lambda_q = 0.52$ cm at the midplane. The total power reaching the divertor plate is 24.5 MW, or 94% of P_{SOL}, as explained above. The maximum electron temperature is 40 eV, the ion temperature is $\simeq$15 eV. The peak density is about 4×10^{20} m^{-3}, and the particle flux at the separatrix intercept is 6×10^{23} s^{-1}. m^{-2}. Integrating the ion flux profile over both upper and lower divertors gives a total loss current $2 \int 2\pi R \Gamma_{i,d} dR = 1.1 \times 10^{24}$ s^{-1}. This compares with a total particle loss across the separatrix of 3.4×10^{22} s^{-1}; the ratio is just $1/(1-r)$.

At the plasma midplane, the density profile is much broader than either the T_e or T_i profiles, as shown in Fig. 9.13. The e-folding length for the reference case is 1.3 cm, but the exact value is sensitive to the boundary conditions at the outer wall and the choice of the inward pinch velocity. Without the pinch, λ_n doubles and the density remains high all the way out to the wall. Since we have no *a priori* reason to expect an inward pinch of this magnitude (the Ware pinch is much smaller), we have also made B2 runs with a sharply lower recycling coefficient on the wall, to simulate the effect of plasma scrape-off on ICRF antenna protection. This produces the dotted midplane profile in Fig. 9.13b and divertor particle flux profile in Fig. 9.12b. Resolving this issue is the subject of continuing work with the B2 code.

The variation of predicted divertor conditions with other input parameters is recorded in Figs. 9.14 and 9.15. The peak divertor heat flux versus power input to the SOL appears in Fig. 9.14a for three different values of χ_e: There

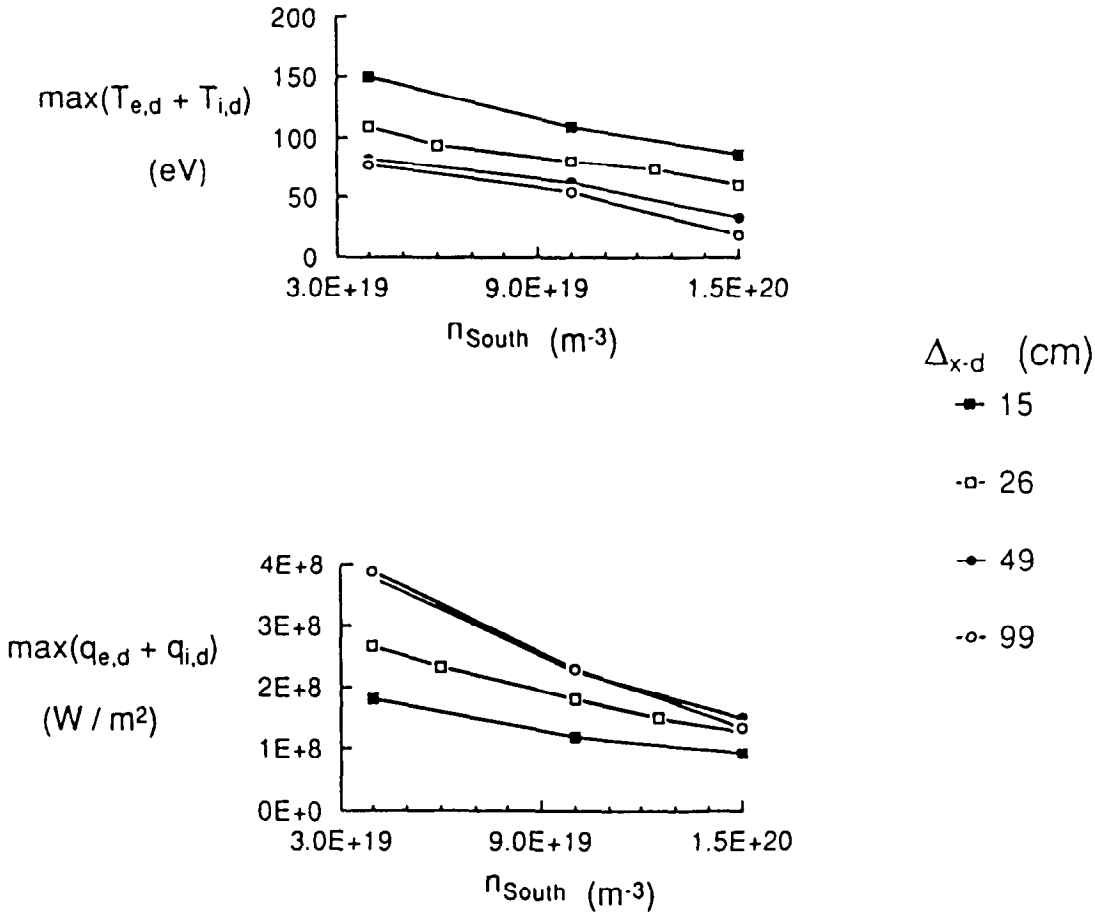

Fig. 9.15. Variation of peak heat flux and plasma temperature with density on the separatrix at the midplane and with X–point to divertor plate distance $\Delta_{x,d}$ for constant total power across the separatrix.

is a $1/\sqrt{\chi}$ dependence as expected. Figure 9.14b shows that the peak $(T_{e,div}+T_{i,div})$ increases as χ is reduced, while the addition of an inward pinch velocity increases the peak temperature by less than 5% .

The influence of the midplane density was examined using B2 runs in which the total power into the SOL was held constant. In this case, the midplane electron temperature varied almost inversely with the density to keep $\Gamma_{E,sep}$ fixed. The output of these runs appears in Fig. 9.15, from which we conclude that increasing edge density reduces the peak divertor heat flux and electron temperature. This results from a drop in parallel heat conduction $(\propto T_e^{7/2})$ associated with the lower SOL temperatures at higher density.

The distance from the X–point to the divertor target can also impact the divertor conditions. Increasing the distance reduces parallel conduction and so lowers the peak $T_{e,div}$. On the other hand, the magnetic flux expansion decreases as one moves farther from the null. So from the heat-flux point of view, closer to the null is better while, from the sputtering point of view, farther away is better. It should also be noted that, as the divertor targets are moved closer to the X–point, the field lines become more parallel to the surface and heat flux peaking due to misalignment will become worse.

IX.E.3. Status of Model Validation

The B2 model has been compared against a limited set of experimental data[41,29,54] from DIII–D, ASDEX, and TFTR. The JET team has focused on using a $1\frac{1}{2}$-dimensional code to model the SOL plasma. They generally find similar values for transport coefficients as have the other groups ($D_\perp \simeq 1$ m^2/s and $\chi_e \simeq 2$ to 3 for ohmic plasmas), but their data for high-power beam-heated plasmas are limited because of heat flux limits on the scanning Langmuir probe that samples the edge plasma. JFT–2M edge plasmas have been modeled using the UEDA two-dimensional code, which

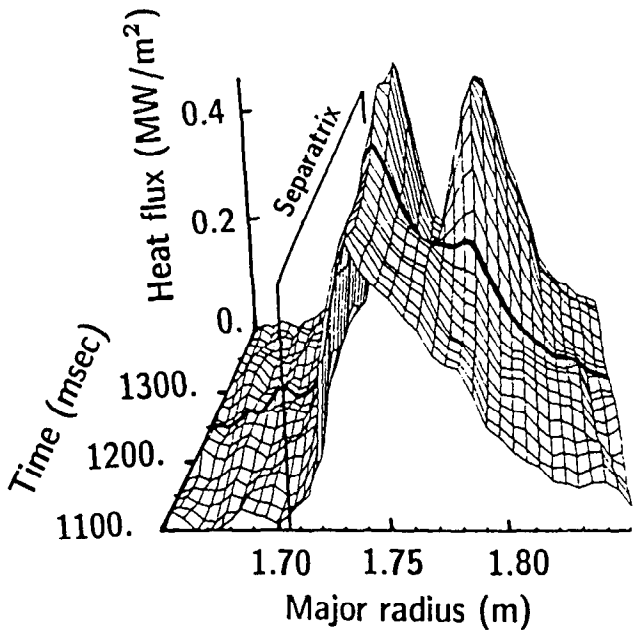

Fig. 9.17. Divertor heat flux profile in DIII–D at the outer separatrix intercept at $\phi = 180$ deg showing the bifurcation produced by a locked mode that starts growing at 1250 ms.

The plasma itself can generate nonaxisymmetric perturbations that affect the divertor heat flux. Nonrotating locked modes can seriously distort the divertor heat flux profile, as shown in Fig. 9.17. In this case, the peak heat flux does not increase, only the total power to the divertor at a given toroidal location. As mentioned earlier, it was reported from ASDEX that ELMing H-mode discharges produced toroidal asymmetries in the total divertor power (not peak heat flux), but it has since been determined that locked modes were responsible.[41] In general, it is easy to discern when locked modes are present, and since they produce disruptive plasmas with poor energy confinement, it seems unlikely that much divertor heating will occur when they are present. Therefore, we include a relatively small "physics safety factor" of 1.2 for plasma and field-error-generated toroidal asymmetries. (Note that ITER chooses 1.5 for this safety factor.) ASDEX data support this, as do the power balance measurements from other divertor tokamaks. Power balance is itself a measure of symmetry because it combines a number of toroidally localized data to compare with the total input power.

Auxiliary heating can also produce toroidal nonuniformity in the divertor heat flux if much of the power is deposited in the edge plasma.[57] In BPX near ignition this would not be the case, so we do not add a safety factor for it.

Other sources of uncertainty for the divertor heat flux have been mentioned in earlier sections. To summarize here: (a) Reducing χ_e by a factor of 2 (lower present data plus Bohm scaling) results in a factor of 1.5 increase in $\hat{q}_d$ due to narrowing of the SOL; (b) assuming a worst-case up-down asymmetry of 2:1 results in a factor of about 1.2 increase in $\hat{q}_d$; and (c) a decrease in $n_{sep}/\hat{n}_e$ from 0.25 to 0.15 (lower bound in present measurements) yields higher heat fluxes by a factor of about 1.3 from B2 simulations, again due to a decrease in λ_q.

Table 9.3 combines these various safety factors into a single factor by which the nominal heat flux is multiplied. Note that factors that increase the peak heat flux by decreasing the width of the SOL have been counted only as the square root (i.e., 1.4 instead of 1.9); this takes into account the benefit of X–point sweeping, which gives the divertor a power handling capability proportional to $(1/\lambda_q)^{1/2}$. Thus, an overall safety factor of 2.7 is obtained. We do not calculate separately the safety factors for the inside and outside strike-points since the outside receives the largest heat flux and both share the same design.

It is worthwhile to note that the approach to determining our confidence level in the predicted peak divertor heat flux is fundamentally different from that used to determine the ignition margin of the device. In that case, regression analysis of a relatively large ensemble of global scaling data was used to predict the machine performance within certain error bars. Also, the number of independent variables is well known and limited (e.g., major and minor radius, plasma current, etc.). In the case of the SOL and divertor plasma parameters, we have been forced by the lack of a similar body of empirical data to resort to calculations using a theoretical model of SOL transport that includes a large number of adjustable parameters that are poorly known (e.g., particle reflection coefficients, sputtering yields, etc.). Unlike the empirical approach, using a model leaves the prediction susceptible to the influence of hidden variables that are not included in the calculation. Thus, to be conservative, we end up multiplying all of the uncertainties to arrive at a worst-case scenario that the design should accommodate.

Taken at face value, a safety factor of 2.7 implies that to have a high degree of confidence in the design, the BPX divertor should be able to handle 27 MW/m^2 peak divertor heat flux when producing 100 MW of fusion power at $Q = 5$. This is feasible using X–point sweeping and state-of-the-art graphites for the divertor modules. On the other hand, it also implies that a "brute-force" high-confidence divertor for BPX at $P_{fus} = 500$ MW

Table 9.3. Peaking Factors and Physics Uncertainties

Source of Uncertainty	Varies Total Power	Varies Width of SOL
Toroidal variations (physics)	1.2	
Toroidal variations (engineering)	1.3	
2:1 Up-down asymmetry (physics)	1.2	
Scaling of transport coefficients		1.5
Other physics scaling (e.g., n_{sep})		1.3
Total multiplicative effect	1.9	1.95 (1.4)
Resulting overall safety factor	2.7	

should be able to handle a worst–case heat flux of about about 54 MW/m^2—surely a formidable engineering task! Therefore, we are considering alternative methods to accommodate a higher than expected heat flux.

First, if the heat heat flux is higher than predicted due to up-down asymmetries, we could dither the vertical balance of the plasma during the discharge to alternately direct more heat to one divertor or the other. The duty cycle of this up-down modulation would be varied to achieve uniform top and bottom heating. Such a modulation should not affect confinement if the heating power is well above the H-mode threshold. A second possibility for accommodating higher than expected heat flux is to shift to an inside–wall limiter configuration after the divertor reaches its temperature limit. If well aligned, the inner wall has a large contact area due to the nearly tangential flux surface intersection with it. Again, based on experimental data, such a configuration should not affect global confinement significantly. This could nearly double the power handling capability of the first wall.

A highly radiative divertor, in which most of the heat flux is dissipated by impurity radiation and charge-exchange losses before it reaches the target plates, also looks like a promising possibility. Recent experiments are showing its feasibility for a tokamak reactor such as BPX. JET has reported[58] that deuterium gas injection below the X–point can delay the onset of carbon blooms by more than two seconds, doubling the total energy throughput of the tokamak. In their experiments, the gas was injected into an ELM–free H-mode discharge, and while global energy confinement was unaffected, the neutron rate fell sharply due to cooling. In DIII–D, D_2 and N_2 injection below the X–point was observed[59] to reduce the divertor heat flux by up to a factor of 3 as shown in Fig. 9.18. In that case, with an ELMing H mode, the gas injection did not reduce the neutron rate significantly and lowered the total stored energy by less than 10%. Laboratory experiments in linear devices have also reported encouraging results at terminating a plasma onto a gas target.[60–62] BPX, because of its relatively short pulse length, would seem to be a prime candidate for such a solution to the heat flux problem. Multiple divertor sweeps provide another possible solution in the case where the peak heat flux has increased due to a reduced scrape-off width.

Finally, it is important to consider that the idea of designing to accommodate the high heat flux resulting from applying the safety factors to the nominal 20 MW/m^2 divertor heat flux is probably the wrong approach to take at this time. The immediate effort should go into reducing these multipliers, as has been proposed in the BPX Physics R & D plan. For example, if it can be shown that plasma- and field-error-generated toroidal asymmetries are not significant, then the safety factor drops from 2.7 down to 2.2, and the worst-case peak heat flux is lowered by 10 MW/m^2. If the up-down asymmetry in DN discharges can be controlled or eliminated, then the worst-case peak heat flux would

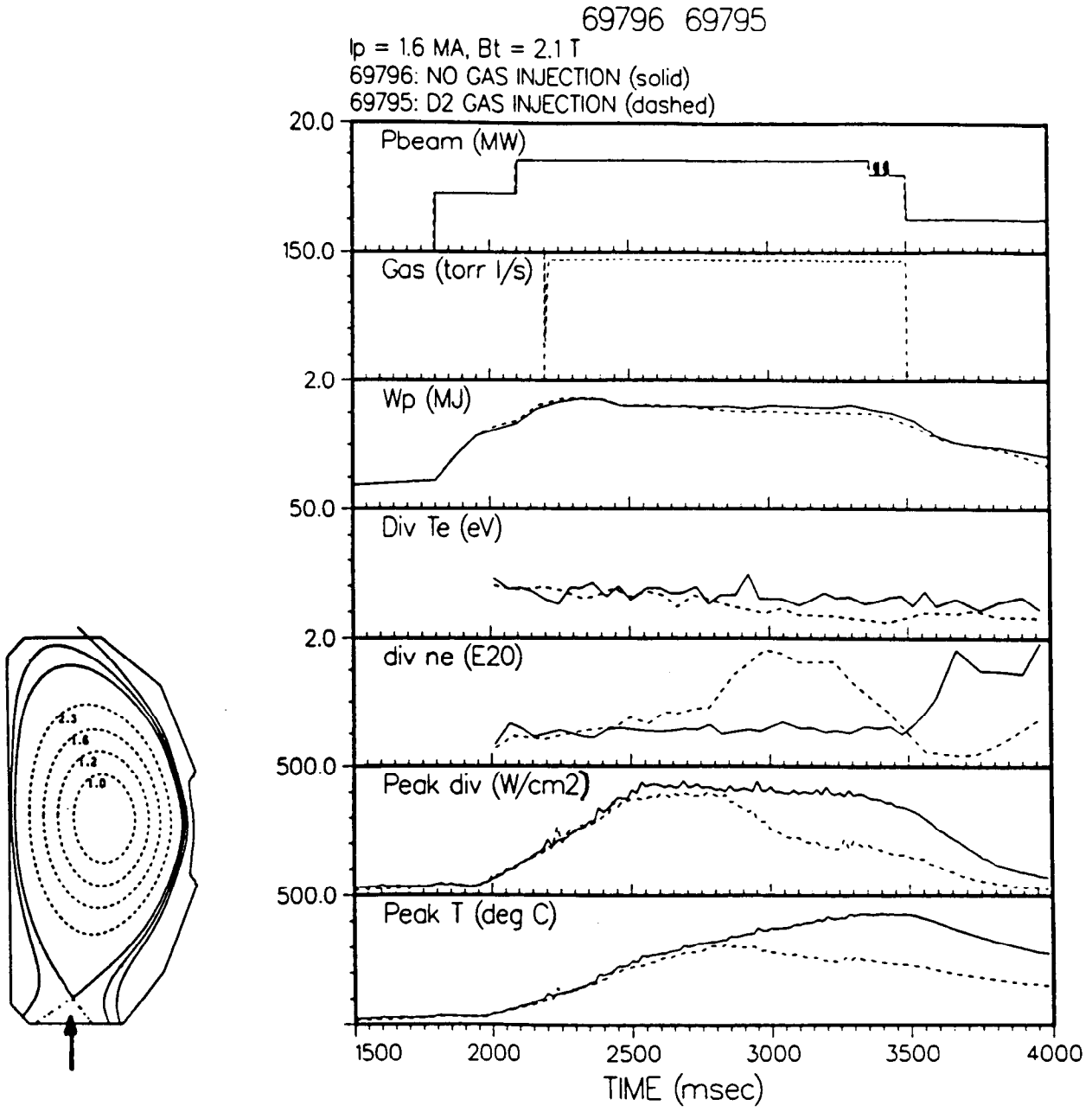

Fig. 9.18. Divertor heat flux reduction in DIII–D by divertor gas injection. Dashed line = 140 Torr-l/s D_2 injection; solid line = no gas injection. The location of the gas injection below the X–point is shown in the small inset.

drop by a similar amount. These goals may not be difficult to achieve since all that is required from the point of view of hardware are a few extra diagnostic views on existing tokamaks and the allocation of experimental run time. The toroidal field scaling of χ is perhaps a more daunting task, but the potential pay-off there is large, too. Thus, we should consider these safety factors as illustrative of the problems to tackle rather than hard limits that must be engineered into the BPX design for $P_{fus} = 500$ MW. In any case, by designing for the nominal $Q = 25$, $P_{fus} = 420$ MW case, we build in sufficient safety margin to accomodate the $Q = 5$, $P_{fus} = 100$ MW case even with all of the uncertainties outlined above.

REFERENCES

1. R. REICHLE, D. D. R. SUMMRS, and M. F. STAMP, Presented at 9th Int. Conf. Plasma Sur-

face Interactions, Bournemouth, UK, May 1990, to be published in *J. Nucl. Mater.*

2. K. ITAMI et al., presented at 9th Int. Conf. Plasma Surface Interactions, Bournemouth, UK, May 1990, to be published in *J. Nucl. Mater.*

3. D. N. HILL et al., *Proc. 13th Int. Conf. Plasma Physics and Controlled Nuclear Fusion Research,* Washington, D. C., October 1–6, 1990, International Atomic Energy Agency (1990).

4. B. J. BRAAMS, "A Multi-Fluid Code for Simulation of the Edge Plasma in Tokamaks," NET Report NR 68 (1987); see also *Fusion Technol.,* **9,** 320 (1986).

5. Y. SHIMOMURA et al., *Nucl. Fusion,* **23,** 869 (1983).

6. I. NAKAZAWA, et al., in *Proc. 16th European Physical Society Conf. Plasma Physics and Controlled Nuclear Fusion,* Venice, Italy, March 13–17, 1989, p. 887.

7. D. R. O'BRIEN et al., *Proc. 17th European Conf. Plasma Physics and Controlled Nuclear Fusion,* Amsterdam, Netherlands, June 25–29, 1990, European Physical Society (1990).

8. G. L. JACKSON et al., *Bull. Am. Phys. Soc.,* **34,** 2115 (1989).

9. G. F. MATTHEWS, D. N. HILL, and M. A. MAHDAVI, "The Angular Dependence of Power in the DIII-D Divertor," GA-A20308, General Atomics (Oct. 1990); to be published in *Nucl. Fusion.*

10. K. ODAJIMA et al., in *Proc. 11th Int. Conf. Plasma Physics and Controlled Nuclear Fusion Research,* Kyoto, Japan, November 13–20, 1986, International Atomic Energy Agency (1987).

11. D. STORK et al., *Bull. Am. Phys. Soc.,* **34,** 2055 (1989).

12. D. N. HILL et al., *Bull. Am. Phys. Soc.,* **33,** 1978 (1988).

13. E. R. MILLER et al., *Proc. 16th European Conf. Plasma Physics and Controlled Nuclear Fusion Research,* Venice, Italy, March 13–17, 1989, p. 257.

14. D. P. SCHISSELL et al., *Nucl. Fusion,* **29,** 185 (1989).

15. A. TANGA et al., *Proc. 13th Int. Conf. Plasma Physics and Controlled Nuclear Fusion Research,* Washington, D. C., October 1–6, 1990, International Atomic Energy Agency (1990).

16. M. A. MAHDAVI et al., *Proc. 16th European Conf. Conf. Controlled Fusion and Plasma Physics,* Venice, Italy, March 13–17, 1989, p. 249.

17. P. GOHIL et al., *Phys. Rev. Lett.,* **61,** 1603 (1988).

18. T. OZEKI et al., *Nucl. Fusion,* **30,** 1425 (1990).

19. M. A. MAHDAVI et al., *J. Nucl. Mater.,* **162-164,** 245 (1989).

20. M. MAYBERRY et al., *Nucl. Fusion,* **30,** 579 (1990).

21. G. FUSSMANN et al., *J. Nucl. Mater.,* **128–129,** 350 (1984).

22. D. N. HILL et al., *Nucl. Fusion,* **28,** 902 (1988).

23. R. D. STAMBAUGH, et al., *Proc. 16th European Conf. on Plasma Physics and Controlled Fusion,* Venice, Italy, March 13–17, 1989.

24. J. NEUHAUSER et al., *Proc. 13th Int. Conf. Plasma Physics and Controlled Nuclear Fusion Research,* Washington, D. C., October 1–6, 1990, International Atomic Energy Atency (1990).

25. R. J. FONCK et al., *J. Nucl. Mater.,* **111–112,** 343 (1982); see also M.G. BELL et al., *J. Nucl. Mater.,* **121,** 132 (1984).

26. E. R. MILLER, M. KEILHACKER, and K. STEINMETZ, *J. Nucl. Mater.,* **121,** 138 (1984).

27. N. MIYA et al., *J. Nucl. Mater.,* **121,** 126 (1984).

28. G. K. McCORMICK et al., *J. Nucl. Mater.,* **162–164,** 264 (1989).

29. D. N. HILL et al., presented at 9th Int. Conf. Plasma Surface Interactions, Bournemouth, UK, May 1990, to be published in *J. Nucl. Mater.*

30. S. A. COHEN et al., "Power and Particle Control," ITER Physics Report, Section 3 (1991).

31. The ASDEX TEAM, *Nucl. Fusion,* **29,** 1959 (1989).

32. S. M. KAYE et al., *J. Nucl. Mater.,* **121,** 115 (1984).

33. S. K. ERENTS et al., *Proc. 17th European Conf. Plasma Physics and Controlled Fusion,* Amsterdam, Netherlands, June 25–29, 1990, p. 1385 (1990).

34. J. D. GALAMBOS and Y.-K. M. PENG, *J. Nucl. Mater.,* **121,** 205 (1984).

35. M. SHIMADA et al., *Phys. Rev. Lett.,* **47,** 796 (1981).

36. M. A. MAHDAVI et al., *J. Nucl. Mater.,* **111 & 112,** 355 (1982).

37. M. SHIMADA et al., *Nucl. Fusion,* **22,** 643 (1982).

38. P. J. HARBOUR, *Nucl. Fusion,* **24,** 1211 (1984).

39. M. F. A. HARRISON, "Impurity Control and Its Impact Upon Startup and Transformer Recharging in NET," CLM-P670, United Kingdom Atomic Energy Authority (1985).

40. P. C. STANGEBY and G.M. MCCRACKEN, *Nucl. Fusion,* **30,** 1225 (1990).

41. J. NEUHAUSER et al., *Plasma Phys. Controlled Nucl. Fusion,* **31,** 1551 (1989).

42. D. E. POST, W. D. LANGER, and M. PETRAVIC, *J. Nucl. Mater.,* **121,** 171 (1984).

43. P. J. HARBOUR et al., *J. Nucl. Mater.,* **162-164,** 236 (1989).

44. D. STOTLER et al., *Bull. Am. Phys. Soc.,* **35,** 1921 (1990).

45. W. A. HOULBERG, S. E. ATTENBERGER, and L. L. LAO, "Computational Methods in Tokamak Tranpsort," ORNL/TM-8193, Oak Ridge National Laboratory (1982).

46. D. A. KNOLL and A. K. PRINJA, *Bull. Am. Phys. Soc.,* **35,** 1987 (1990).

47. S. A. KAHN and T. D. ROGNLIEN, *Phys. Fluids* **24,** 1442 (1981); see also T. D. ROGNLIEN, *Bull. Am. Phys. Soc.,* **34,** 1981 (1989).

48. M. J. SCHAFFER and B. J. LEIKIND, "Observation of Electric Currents in Diverted Tokamak Scrape-Off Layers," GA-A20128, General Atomics (1991).

49. G. M. STAEBLER and F. L. HINTON, *Nucl. Fusion,* **29,** 1820 (1989).

50. N. UEDA et al., *J. Nucl. Mater.,* **162–164,** 607 (1989).

51. G. M. STAEBLER, "Transport Modeling of Divertor Bias Experiments," GA-A20185, General Atomics (1990).

52. T. D. ROGNLIEN et al., "Modeling Cross-Field Drifts and Current With the B2 Code for the CIT Divertor," UCRL-ID-105272, Lawrence Livermore National Laboratory (Nov. 1990).

53. R. B. CAMPBELL, D. A. KNOLL, and A. K. PRINJA, *Bull. Am. Phys. Soc.,* **35,** 1987 (1990).

54. D. P. COSTER et al., *Bull. Am. Phys. Soc.,* **35,** 2086 (1990).

55. M. ULRICKSON et al., presented at 9th Int. Conf. Plasma Surface Interactions, Bournemouth, UK, May 1990, to be published in *J. Nucl. Mater.*

56. B. L. DOYLE, J. B. WHITLEY, and K. L. WILSON, Eds., "Magnetic Fusion Energy Program Annual Report," p. 43, Sandia National Laboratories (1989).

57. R. LaHAYE, "Calculation of the Effects of Field Errors on Diverted Magnetic Field," GA-A20327, General Atomics, (1991); see also J. T. SCOVILLE et al., "A Discussion of Locked Modes in DIII–D and a Method for Prevention of the Low Density Mode," GA-A19983, General Atomics (1990).

58. T. E. EVANS and the ASDEX TEAM, presented at 9th Int. Conf. on Plasma Surface Interactions, Bournemouth, UK, May 1990, to be published in *J. Nucl. Mater.*

59. D. STORK et al., *Bull. Am. Phys. Soc.,* **34,** 2055 (1989).

60. T. W. PETRIE et al., *Bull. Am. Phys. Soc.,* **35,** 2024 (1990).

61. W. L. HSU, M. YAMADA, and P. J. BARRETT, *Phys. Rev. Lett.,* **49,** 1001 (1982).

62. G. FIKSEL, M. KISHINEVSKY, and N. HERSHKOWITZ, *Phys. Fluids B,* **2,** 837 (1989).

63. L. SCHMITZ et al., presented at 9th Int. Conf. on Plasma Surface Interactions, Bournemouth, UK, May 1990, to be published in *J. Nucl. Mater.*